scientific reports

Check for updates

OPEN

Design and performance optimization of circularly polarized luminescent materials based on lanthanide helicates

Xiumei Zhang[1,2,3], Xinglu Wang[1,3], Wenru Huang[1], Sen Yin[1], Ting Gao[1], Yanyan Zhou[1]✉ & Hongfeng Li[1]✉

Chiral lanthanide complexes, due to their high luminescence dissymmetry factor (g_{lum}) and luminescent quantum yield, have become highly promising materials for circularly polarized luminescence (CPL). Herein, we report two novel pairs of lanthanide chiral complexes, which exhibit both a high g_{lum} and high luminescence quantum efficiency. Photophysical and chiroptical investigations revealed that both $(NEt_4)_2[Eu_2(L_1{}^S)_4]$ and $(NEt_4)_2[Eu_2(L_2{}^S)_4]$ displayed intense CPL. Their g_{lum} values for $^5D_0 \rightarrow {}^7F_1$ transition reach + 1.34 and + 1.14, respectively, exhibiting high luminescence quantum yields of 37.43% and 30.30% for $^5D_0 \rightarrow {}^7F_J$ transitions (J = 0 – 4). Through the analysis of the photophysical properties and X-ray single-crystal structures of $(NEt_4)_2[Eu_2(L_1{}^S)_4]$ and $(NEt_4)_2[Eu_2(L_2{}^S)_4]$, it was found that the modification of the ligand significantly affected the twist angle α of the coordination polyhedron, revealing the direct cause for achieving a high g_{lum}. This study provides a new design concept for the development of other lanthanide-based CPL materials with high g_{lum} values and high luminescence quantum yields.

Keywords Binaphthol, β-diketones, Lanthanide complexes, Helicate, Crystal structure, CPL

In recent years, chiral lanthanide supramolecules with circularly polarized luminescence (CPL) properties have attracted great attention due to their potential applications in three-dimensional (3D) displays[1–4], information storage[5–9], CPL probes[10–14], asymmetric synthesis[15–17]. The luminescence dissymmetry factor (g_{lum}) along with the luminescence quantum yields (QYs) constitutes two crucial parameters when it comes to evaluating the performance of these materials. Due to the magnetic dipole transition characteristics of some lanthanide ions Ln(III), the g_{lum} values of the lanthanide luminescent materials are obviously higher than those of other luminescent systems, such as organic molecules[18,19], polymers[20,21], supramolecules[22,23], and transition-metal complexes[24,25]. For instance, in 2008, Muller et al. reported a mononuclear chiral lanthanide complex Cs[Eu((+)-hfbc)$_4$], whose g_{lum} value was as high as + 1.38[26]. This work surpassed the g-value of circularly polarized materials at the time; however, its luminescence efficiency in chloroform was only 0.6%. Therefore, the inability to simultaneously achieve high g_{lum} values and high luminescence quantum yields limits its application in lanthanide-based CPL materials. Subsequently, researchers developed a series of Eu-based circularly polarized luminescent materials with excellent luminescent performance. For example, Md.J. Islam et al[27]. reported the circularly polarized properties of $[Eu(tfc)_3(DPO)_2]$ $(H_2O)_2$, with a g-value as high as 0.025, but a relatively low PLQY of 4.09%. They attributed the low PLQY to the metal-to-ligand back electron transfer (LMBET) process. Francesco et al[28]. reported three new Eu-based circularly polarized materials with excellent performance, all of which exhibited PLQYs of 30% in solution and g_{lum} of approximately 0.77, 0.75, and 0.22, respectively. In many materials, a high g_{lum} is typically associated with a low PLQY. This phenomenon is primarily attributed to the competitive mechanisms involved in the emission process: as the g-value increases, non-radiative recombination processes (such as LMBET, thermal excitation) may be enhanced, leading to a reduction in PLQY. Consequently, the interplay between the g_{lum} and PLQY has become a central topic in the current research on circularly polarized luminescent materials.

[1]Key Laboratory of Functional Inorganic Material Chemistry, Ministry of Education, School of Chemistry and Materials Science, Heilongjiang University, 74 Xuefu Road, Harbin 150080, China. [2]School of Pharmacy, Jiamusi University, Jiamusi 154007, China. [3]Xiumei Zhang and Xinglu Wang contributed equally to this work. ✉email: zhouyanyan@hlju.edu.cn; lihongfeng@hlju.edu.cn

The pursuit of high PLQY remains a central focus in the design of CPL materials[29]. According to existing studies, β-diketones are extensively employed as ligands in luminescent lanthanide complexes due to their ability to efficiently sensitize lanthanide ions, including visible-emitting Eu(III)[30–32] and Sm(III)[33], as well as near-infrared-emitting Nd(III)[34], Er(III)[35,36], and Yb(III)[37]. In addition to PLQY, another crucial factor to consider in the development of CPL materials is the enhancement of the g_{lum} value. Although no universally applicable relationship has been established between g_{lum} and the structures of chiral lanthanide complexes, it is generally believed that high g_{lum} values are associated with the rigidity and high symmetry of the complexes. For instance, our research group reported a g_{lum} value of 0.81 for a pair of ytterbium helicates, $[Yb_2(R/S\text{-}BTHP)_4]^{2-}$, the highest value reported for Yb-based CPL materials to date[38]. Additionally, the Hasegawa research group reported a g_{lum} value of 1.54 for chiral tetrakis-Eu(III) complexes, the highest value reported for chiral luminescent molecules[39].

Building upon the aforementioned considerations, we designed and synthesized two pairs of enantiopure bis-β-diketones, $\mathbf{L_1}^{R/S}$ and $\mathbf{L_2}^{R/S}$, which self-assemble with Eu(III) ions in a 2:1 molar ratio, resulting in the formation of quadruple-stranded helicates, $(NEt_4)_2[Eu_2(\mathbf{L_1}^{S})_4]$ and $(NEt_4)_2[Eu_2(\mathbf{L_2}^{S})_4]$ (Scheme 1). Comprehensive spectroscopic analysis confirmed the successful formation of these quadruple-stranded helicates. Single-crystal X-ray diffraction analysis revealed that the coordination environments of the two Eu(III) metal centers in both $(NEt_4)_2[Eu_2(\mathbf{L_1}^{S})_4]$ and $(NEt_4)_2[Eu_2(\mathbf{L_2}^{S})_4]$ exhibit a fully symmetric square antiprismatic geometry. Chiroptical property measurements demonstrated that $(NEt_4)_2[Eu_2(\mathbf{L_1}^{S})_4]$ exhibits remarkable CPL activity, with a g_{lum} value of + 1.34 and a QYs of 37.19%. In contrast, $(NEt_4)_2[Eu_2(\mathbf{L_2}^{S})_4]$ shows relatively weaker CPL activity, with a g_{lum} value of + 1.14 and a QYs of 30.30%.

Materials and methods

NMR and ESI-TOF–MS

The ^1H NMR, ^{19}F NMR and ^1H-^1H DOSY spectra were recorded on a Bruker AVANCE III 400 MHz spectrometer. ^1H NMR chemical shifts are in ppm relative to tetramethylsilane (TMS): $CDCl_3$ (7.26 ppm for ^1H), CD_3CN (1.94 ppm for ^1H).

High-resolution electrospray ionization mass spectrometry (ESI-TOF–MS) were recorded by using a Bruker maXis mass spectrometer. Data analysis was conducted with the Mass-Lynx Data Analysis software (Version 4.1) and simulations were performed with the MassLynx Isotope Pattern software.

FT-IR spectra measurements

FT-IR spectra of all samples were performed with a Perkin Elmer Spectrum One spectrophotometer by using KBr disks in the range of 4000 – 370 cm^{-1}.

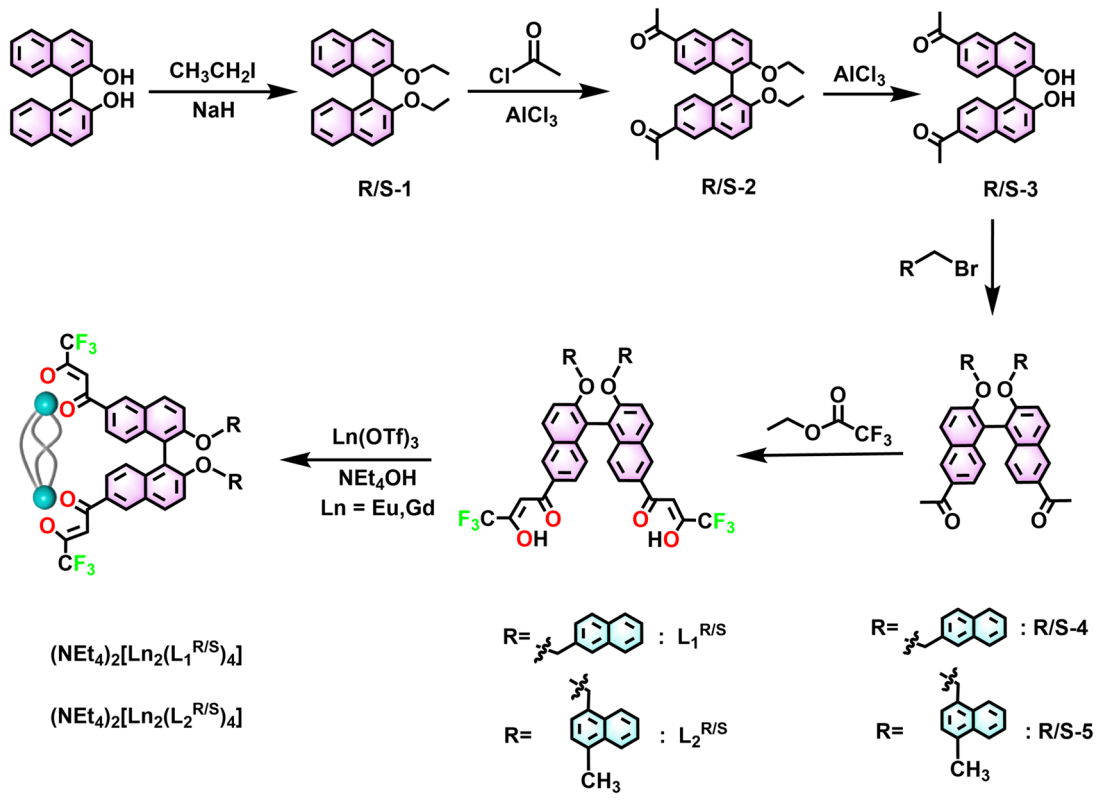

Scheme 1. Synthetic routes of the $\mathbf{L_1}^{R/S}$, $\mathbf{L_2}^{R/S}$ and corresponding lanthanide complexes, $(NEt_4)_2[Ln_2(\mathbf{L_1}^{R/S})_4]$ and $(NEt_4)_2[Ln_2(\mathbf{L_2}^{R/S})_4]$ (Ln = Eu and Gd).

Photophysical behavior

UV–vis spectra were recorded in CH_3CN ($c = 1.0 \times 10^{-5}$ M) at room temperature in 10 mm light path quartzcuvettes on a PerkinElmer Lambda 25 spectrometer.

Excitation and emission spectra were recorded using an Edinburgh FLS 980 fluorescence spectrometer equipped with a red-sensitive photomultiplier detector (Hamamatsu R928). Excitation spectra were measured in CH_3CN ($c = 1.0 \times 10^{-5}$ M) with quartz cuvettes of 10 mm path length. Emission spectra were measured in CH_3CN ($c = 1.0 \times 10^{-5}$ M) with quartz cuvettes of 10 mm path length.

Luminescence lifetimes were recorded on a single photon counting spectrometer from Edinburgh Instruments (FLS 980) with a microsecond pulse lamp as the excitation source.

The luminescence quantum yields (Φ) of the samples were recorded at room temperature through an absolute method using an Edinburgh Instruments integrating sphere coupled to the modular Edinburgh FLS 980 fluorescence spectrometer. The absolute quantum yield was calculated using the following expression:

$$\Phi = \frac{\int L_{emission}}{\int E_{reference} - \int E_{sample}} \tag{1}$$

Where $L_{emission}$ is the emission spectrum of the sample, collecting using the sphere, E_{sample} is the spectrum of the incident light used to excite the sample, collected using the sphere, and $E_{reference}$ is the spectrum of the light used for excitation with only the reference in the sphere. The method is accurate within 10%.

$$k_r = \frac{1}{\tau_{rad}} = A_{MD,\,0} n^3 \left(\frac{I_{tot}}{I_{MD}}\right) \tag{2}$$

The radiative rate constant (k_r) is proportional to the intensity ratio of total integrated emission of the $^5D_0 \rightarrow {}^7F_J$ transitions (I_{tot}) to the integrated emission of the $^5D_0 \rightarrow {}^7F_1$ transitions (I_{MD}). $A_{MD,0}$ (14.65 s^{-1}) is the spontaneous emission probability of the $^5D_0 \rightarrow {}^7F_1$ transition and n is the refractive index of the medium.

The radiative transition (k_r) values and non-radiative transition (k_{nr}) determine the intrinsic quantum yield (Φ_{Ln}) of Eu^{3+} ion emission as shown in Eq. (3).

$$\Phi_{Ln} = \frac{k_r}{k_r + k_{nr}} = \frac{\tau_{obs}}{\tau_{rad}} \tag{3}$$

T_{obs} is the observed lifetimes. On the basis of the emission decay curves monitored within the $^5D_0 \rightarrow {}^7F_2$ transition. The sensitization efficiencies (ηsen) can be calculated.

$$\Phi_{overall} = \eta_{sen} \Phi_{Ln} \tag{4}$$

Chiraloptical measurements

CD and CPL experiments were performed on an Olis DM245 spectrometer at room temperature. All samples were dissolved in CH_3CN ($c = 1.0 \times 10^{-5}$ M), and quartz cuvettes with optical pathway of 10 mm were employed. CD spectra were recorded in the range of 250 − 450 nm in increments of 1 nm, and a slit width of 2 mm for the excitation was utilized. CPL spectra were recorded with a 375 nm laser as light source. The emission of left- and right-handed polarized light were collected in the range of 550 − 720 nm with the integration time of 1 s and the emission slit width of 0.6 mm.

X-ray crystallography

Crystallographic data of $(NEt_4)_2[Eu_2(\mathbf{L_1^S})_4]$ and $(NEt_4)_2[Eu_2(\mathbf{L_2^S})_4]$ are given in Table S3 and Table S4. Single crystals of suitable dimensions of $(NEt_4)_2[Eu_2(\mathbf{L_1^S})_4]$ and $(NEt_4)_2[Eu_2(\mathbf{L_2^S})_4]$ were selected for single-crystal X-ray diffraction analysis. Crystallographic data were collected at 140 K and 150 K on a Xcalibur, Eos, Gemini diffractometer with Mo Kα radiation (λ = 0.71073 Å). The structures were solved by direct methods and refined by the full-matrix least-squares method based on F^2 with anisotropic gthermal parameters for all non-hydrogen atoms by using the SHELXS (direct methods) and refined by SHELXL 2018[40] (full matrix least-squares techniques) in the Olex2 package[41]. The crystallographic data in CIF format were deposited at the Cambridge Crystallographic Data Centre with CCDC Nos. 2410043 and Nos. 2362879. These data are available free of charge from the Cambridge Crystallographic Data Centre, 12 Union Road, Cambridge CB21 EZ, UK; fax: (+ 44) 1223–336-033; or e-mail: deposit@ccdc.cam.ac.uk.

Results and discussion

Syntheses and characterization

The synthetic procedures of the ligands ($\mathbf{L_1^{R/S}}$ and $\mathbf{L_2^{R/S}}$) and their characterization ESI-TOF–MS and ^1H, ^{19}F NMR are given in the ESI (Schemes S1 − S2 and Figures S1 − S18). To obtain the $(NEt_4)_2[Eu_2(\mathbf{L^S})_4]$ helicates, the ligands $\mathbf{L_1^S}$ and $\mathbf{L_2^S}$ were assembled with $Eu(OTf)_3$ in a 2:1 stoichiometric ratio with tetraethylammonium hydroxide (NEt_4OH) as the base in CH_3CN, respectively, as shown in Fig. 1 a and 1b (Figures S19 − S30). ESI-TOF–MS analyses affirmed the formation of the quadruple-stranded helicates of $(NEt_4)_2[Eu_2(\mathbf{L_1^{R/S}})_4]$ and $(NEt_4)_2[Eu_2(\mathbf{L_2^{R/S}})_4]$. For instance, in the negative ionization mode, both Fig. 1 c and 1 d display a cluster of peaks, which can be attributed to the charged $[Eu_2(\mathbf{L^S})_4]^{2-}$ ($\mathbf{L^S} = \mathbf{L_1^S}$, $\mathbf{L_2^S}$) at m/z 1833.0378, 1889.6063, respectively. Furthermore, the ^1H and ^{19}F analyses (Figures S31 − S32) also support the formation of the quadruple-stranded

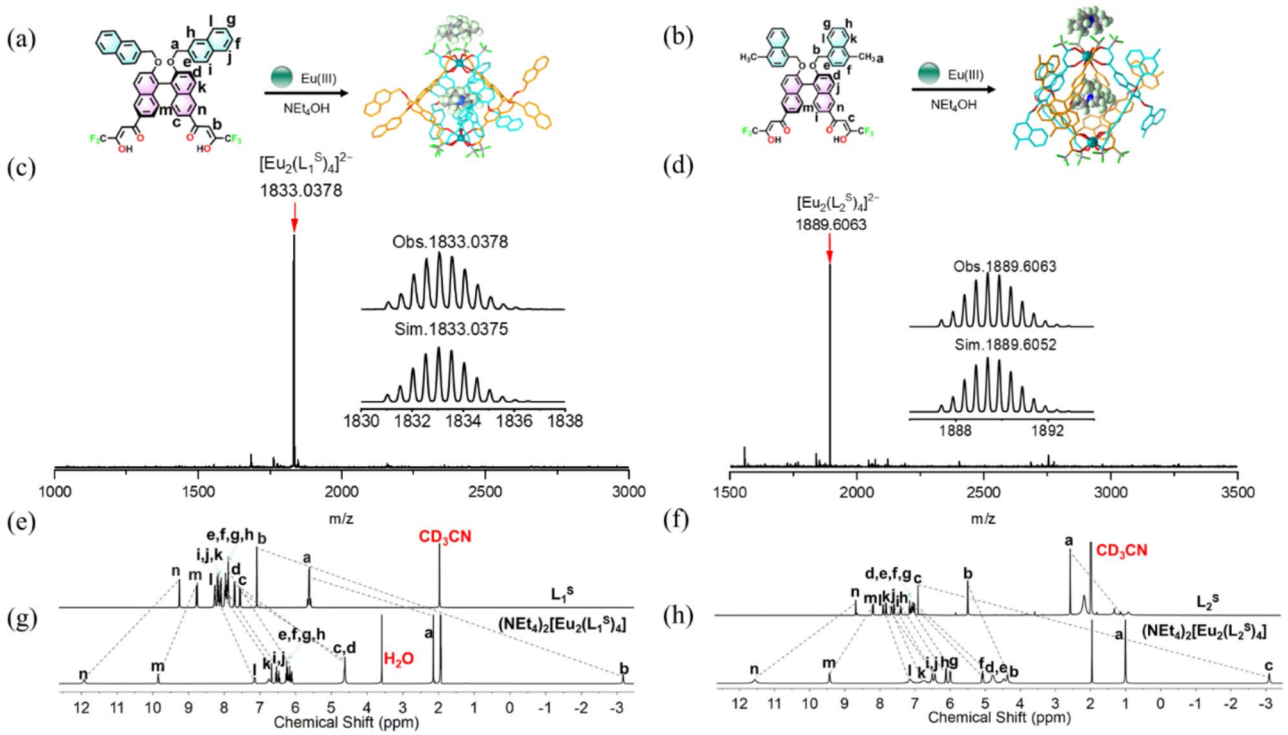

Fig. 1. Synthesis and characterization of complexes. Self-assembly of quadruple-stranded Eu(III) helicates by the ligands $\mathbf{L_1}^{\mathbf{S}}$ (**a**) and $\mathbf{L_2}^{\mathbf{S}}$ (**b**). ESI-TOF–MS spectrum of $(NEt_4)_2[Eu_2(\mathbf{L_1}^{\mathbf{S}})_4]$ (**c**) and $(NEt_4)_2[Eu_2(\mathbf{L_2}^{\mathbf{S}})_4]$ (**d**). ^{1}H NMR (400 MHz) spectra of $\mathbf{L_1}^{\mathbf{S}}$ (**e**), $\mathbf{L_2}^{\mathbf{S}}$ (**f**), $(NEt_4)_2[Eu_2(\mathbf{L_1}^{\mathbf{S}})_4]$ (**g**) and $(NEt_4)_2[Eu_2(\mathbf{L_2}^{\mathbf{S}})_4]$ (**h**) in CD_3CN.

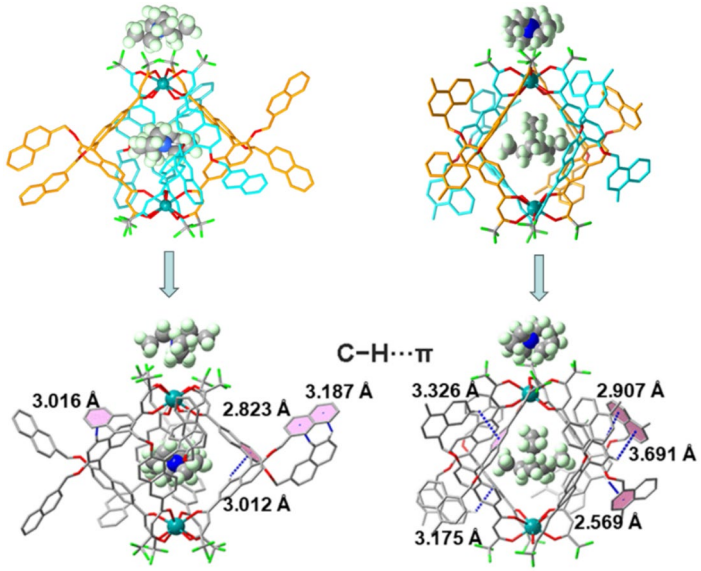

Fig. 2. X-ray single crystal structures of the helicates and C-H···π interaction of $(NEt_4)_2[Eu_2(\mathbf{L_1}^{\mathbf{S}})_4]$ and $(NEt_4)_2[Eu_2(\mathbf{L_2}^{\mathbf{S}})_4]$. (color code for Eu: cyan, N: blue, F: green, and O: red) Hydrogen atoms on the helicates are omitted for clarity.

helicates of $(NEt_4)_2[Eu_2(\mathbf{L}^{\mathbf{S}})_4]$. In contrast to the free ligands $\mathbf{L}^{\mathbf{S}}$ (Fig. 1 e and 1f.), all resonance peaks in $(NEt_4)_2[Eu_2(\mathbf{L}^{\mathbf{S}})_4]$ show shifts and a slight increase in width, but the splitting of the peaks is still distinguishable without difficulty (Fig. 1 g and 1 h).

X-ray crystallography analysis provides strong evidence for the formation of quadruple-stranded helicates, and the complexes $(NEt_4)_2[Eu_2(\mathbf{L_1}^{\mathbf{S}})_4]$ and $(NEt_4)_2[Eu_2(\mathbf{L_2}^{\mathbf{S}})_4]$ were crystallized in the chiral space groups *P*1 (Fig. 2). The high quality, block-shaped crystals suitable for single crystal X-ray analysis were obtained by slow

evaporation of the acetonitrile/1,4-dioxane solution of $(NEt_4)_2[Eu_2(\mathbf{L_1}^{S})_4]$ and $(NEt_4)_2[Eu_2(\mathbf{L_2}^{S})_4]$ at room temperature. In $(NEt_4)_2[Eu_2(\mathbf{L_1}^{S})_4]$ and $(NEt_4)_2[Eu_2(\mathbf{L_2}^{S})_4]$, each Eu^{3+} ion is eight-coordinated to O atoms from four β-diketonate ligands. In each helicate, the S-BINOL spacer imparts the assembly with P-helical chirality and homochiral ΔΔ configuration of the two metal centers for $(NEt_4)_2[Eu_2(\mathbf{L_1}^{S})_4]$ and $(NEt_4)_2[Eu_2(\mathbf{L_2}^{S})_4]$ (Figures S33-S36 and Tables S1-S4).

Optical/chiroptical properties

On the basis of X-ray single crystal structures, in combination with the NMR analyses, it is proposed that the preorganized helical chirality of the ligands effectively promotes the formation of homochiral helicates. Therefore, the helical chirality of the $(NEt_4)_2[Eu_2(\mathbf{L}^{R/S})_4]$ ($\mathbf{L}^{R/S}=\mathbf{L_1}^{R/S}$ and $\mathbf{L_2}^{R/S}$) was initially examined using circular dichroism (CD) spectroscopy. As shown in Figs. 3a and 3b, $(NEt_4)_2[Eu_2(\mathbf{L_1}^{R/S})_4]$ and $(NEt_4)_2[Eu_2(\mathbf{L_2}^{R/S})_4]$ exhibit mirror-image Cotton curves in the range of 250–450 nm in CH_3CN, respectively, corresponding to the $\pi-\pi^*$ transition of the free ligands $\mathbf{L}^{R/S}$. These results indicate that both complexes have a high enantiomeric purity. According to the empirical relationship between the exciton coupling pattern and the absolute configuration of the metal center[42–47], we observed that the relationship between the CD exciton coupling signals of $(NEt_4)_2[Eu_2(\mathbf{L_1}^{S})_4]$ and $(NEt_4)_2[Eu_2(\mathbf{L_2}^{S})_4]$ and the absolute configuration of the lanthanide Eu(III) ion centers in their single crystal structures is consistent with the empirical rules reported in the literature. In $(NEt_4)_2[Eu_2(\mathbf{L_1}^{S})_4]$ and $(NEt_4)_2[Eu_2(\mathbf{L_2}^{S})_4]$, the S-BINOL spacer imparts the assembly with P-helical chirality and homochiral ΔΔ configuration to the two metal centers.

Lanthanide elements have an unfilled 4f. electron orbital and a filled $5s^25p^6$ electron orbital, where the 4f electron is located in the $5s^25p^6$ shell. This provides the possibility for electrons to transition between different energy levels. Due to the role of electron shielding, 4f. electrons are less affected by the external field, which makes the rare earth complexes formed after the coordination of rare earth ions and ligands show relatively sharp emission bands. The PL spectra of $(NEt_4)_2[Eu_2(\mathbf{L_1}^{R/S})_4]$ and $(NEt_4)_2[Eu_2(\mathbf{L_2}^{R/S})_4]$ in CH_3CN are shown in Figs. 3c and 3d. The Eu(III) ions in both cases exhibit five characteristic emission bands at 579 nm, 593 nm, 613 nm, 652 nm and 701 nm, corresponding to $^5D_0\rightarrow{}^7F_J$ (J = 0–4) transitions, are observed. In addition, the $^5D_0\rightarrow{}^7F_1$ (magnetic dipole transition) and $^5D_0\rightarrow{}^7F_2$ (electric dipole transition) exhibit stronger emission intensity than $^5D_0\rightarrow{}^7F_{0,3,4}$. Although the total emission intensity of the $^5D_0\rightarrow{}^7F_1$ transition is low, its magnetic dipole character still shows the strongest circularly polarized emission. As expected, the $(NEt_4)_2[Eu_2(\mathbf{L_1}^{R/S})_4]$ and $(NEt_4)_2[Eu_2(\mathbf{L_2}^{R/S})_4]$ exhibit mirror-image CPL emission at the corresponding bands observed in the PL

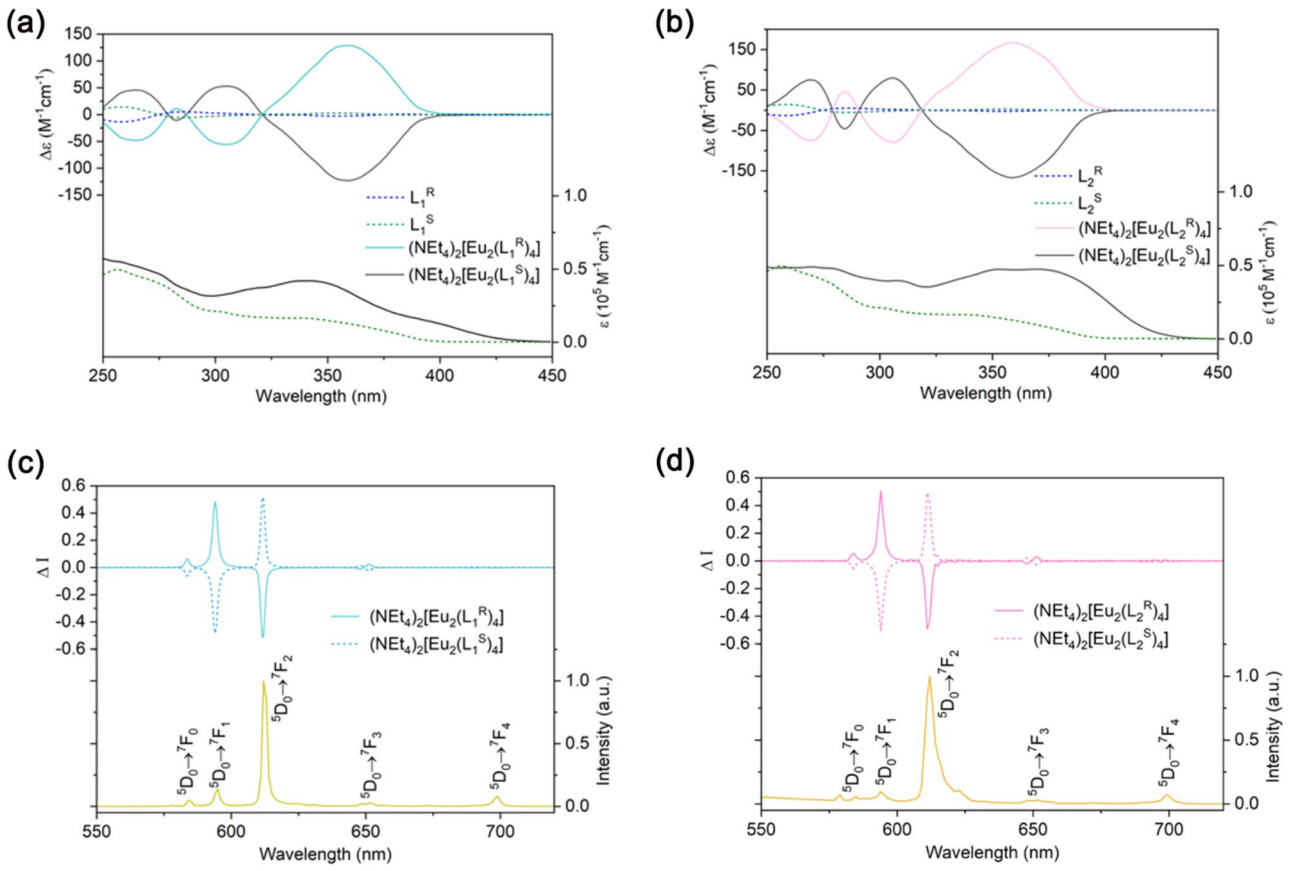

Fig. 3. (**a**) UV–vis and CD spectra of the free ligands and their helicates $(NEt_4)_2[Eu_2(\mathbf{L_1}^{R/S})_4]$ and (**b**) $(NEt_4)_2[Eu_2(\mathbf{L_2}^{R/S})_4]$. (**c**) total emission and CPL spectra of the enantiomeric helicates $(NEt_4)_2[Eu_2(\mathbf{L_1}^{R/S})_4]$ and (**d**) $(NEt_4)_2[Eu_2(\mathbf{L_2}^{R/S})_4]$ in CH_3CN ($c = 1.0\times10^{-5}$ M).

spectrum. G_{lum} value is an essential parameter for estimating the degree of CPL, and $g_{lum} = 2(I_L - I_R)/(I_L + I_R)$, where I_L and I_R represent the left and right circularly polarized emission intensities, respectively (with $-2 \leq g_{lum} \leq 2$). At the magnetic dipole $^5D_0 \rightarrow {}^7F_1$ transition of 595 nm, $(NEt_4)_2[Eu_2(\mathbf{L_1}^{S})_4]$ and $(NEt_4)_2[Eu_2(\mathbf{L_2}^{S})_4]$ exhibit the g_{lum} value of + 1.34 and + 1.14. Notably, the g_{lum} value of $(NEt_4)_2[Eu_2(\mathbf{L_1}^{S})_4]$ is close to the highest recorded g_{lum} value of 1.54 for compounds in solution. Meanwhile, the calculated intensity ratio of $(^5D_0 \rightarrow {}^7F_2)/(^5D_0 \rightarrow {}^7F_1)$ is 10.52 for $(NEt_4)_2[Eu_2(\mathbf{L_1}^{S})_4]$ and 7.14 for $(NEt_4)_2[Eu_2(\mathbf{L_2}^{S})_4]$, respectively, that is, the lower the symmetry of the coordination environment in $(NEt_4)_2[Eu_2(\mathbf{L_1}^{S})_4]$.

The photophysical properties of the $(NEt_4)_2[Eu_2(\mathbf{L_1}^{R/S})_4]$ and $(NEt_4)_2[Eu_2(\mathbf{L_2}^{R/S})_4]$ were further characterized by steady state and transient state spectral measurements (Figures S37 – 44), with the calculated results listed in Table S5 and S6. Overall, both $(NEt_4)_2[Eu_2(\mathbf{L_1}^{R/S})_4]$ and $(NEt_4)_2[Eu_2(\mathbf{L_2}^{R/S})_4]$ have high g_{lum} values and luminescent quantum yields in CH_3CN, establishing them among the most comprehensively performing rare earth CPL materials. The excited-state lifetimes of the Eu(III) ion by monitoring the decay curves of the maxima emission at 613 nm were found to be 570.41 µs, 575.33 µs, 540.61 µs, and 540.74 µs for $(NEt_4)_2[Eu_2(\mathbf{L_1}^{R/S})_4]$ and $(NEt_4)_2[Eu_2(\mathbf{L_2}^{R/S})_4]$ in acetonitrile, respectively (Figures S45 – 46).

On the other hand, the luminescence quantum yield is another essential parameter to evaluate the performance of the CPL materials. The triplet energy level estimated from the maximum emission band (497 and 499 nm) of the corresponding Gd(III) complex was calculated to be 20,120 and 20,040 cm^{-1} for $(NEt_4)_2[Gd(\mathbf{L_1}^{S})_4]$ and $(NEt_4)_2[Gd_2(\mathbf{L_2}^{S})_4]$ (Figures S47-S48). Considering the relatively low energy gap ΔE (T_1-$^5D_0$, 2620 and 2540 cm^{-1}) between the triplet-state energy level of the ligands and the $^5D_0$ energy level of the Eu^{3+} ion (17,500 cm^{-1}), all are within the optimal range of energy transfer. Both $(NEt_4)_2[Eu_2(\mathbf{L_1}^{S})_4]$ and $(NEt_4)_2[Eu_2(\mathbf{L_2}^{S})_4]$ emit bright red light in CH_3CN, with luminescence quantum yields of 37.43% and 30.30% respectively.

To investigate the luminescence mechanism of the complexes, the HOMO and LUMO distribution of the two helicates were calculated by Time-dependent density functional theory calculation (DFT). As shown in Fig. 4, the HOMO and LUMO localized on the chiral ligands, this is the source of the CPL of the helicates. In addition, the HOMO orbital is localized on the binaphthol, while the LUMO orbital locates on the β-diketone moiety. This result confirms the participation of the BINOL moiety on HOMO → LUMO electron transition.

Origin analysis of the strong CPL

From a theoretical perspective, the g_{lum} can be calculated using the equation: $g_{lum} = 4(|\mu| \times |m| \times \cos\theta_{\mu,m})/(|\mu|^2 + |m|^2)$,where µ, *m* and $\theta_{\mu,m}$ represent the electric and magnetic transition dipole moments, and the angle between them, respectively. To achieve a high g_{lum} value, the electron transition must balance the electric and magnetic dipole moments, forming an ideal angle between them. In contrast to organic compounds, the partial f–f transitions of Ln^{3+} ions are allowed as magnetic dipole transitions, such as the $^5D_0 \rightarrow {}^7F_1$ transition of Eu(III) ions. This typically endows chiral lanthanide complexes with exceptionally high CPL activity, often resulting in g_{lum} values that are 2–3 orders of magnitude higher than those observed in organic luminophores.

For lanthanide metals, the f–f transitions are intraconfigurational and Laporte-forbidden. To achieve strong CPL emission, the lanthanide center requires a dissymmetric ligand field that can mix the 4f. and 5 d orbitals to generate the required electric (µ) and magnetic (m) transition dipole moments. In this process, the rigidity of the complex's conformation plays a crucial role in determining the extent of mixing at the dipole transition[48]. The ligands we designed are modified with two naphthalene rings based on S-BINOL. We anticipate strong C-H···π

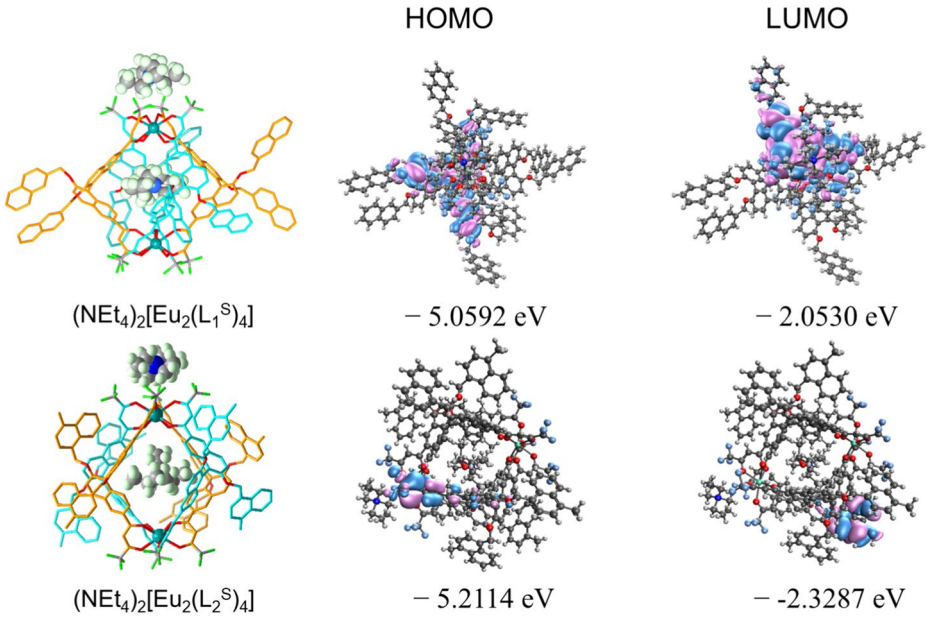

Fig. 4. Schematic diagram showing the electronic density contours for the HOMO, and LUMO molecular orbitals of the $(NEt_4)_2[Eu_2(\mathbf{L_1}^{S})_4]$ and $(NEt_4)_2[Eu_2(\mathbf{L_2}^{S})_4]$.

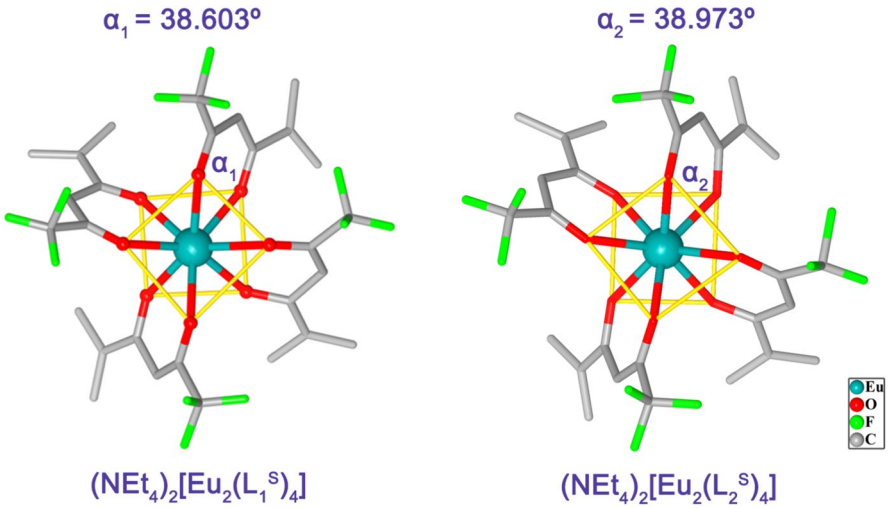

Fig. 5. The torsion angle between the two planes of the SAPR coordination polyhedron of $(NEt_4)_2[Eu_2(\mathbf{L_1}^S)_4]$ and $(NEt_4)_2[Eu_2(\mathbf{L_2}^S)_4]$.

interactions in the complexes formed by these ligands, which significantly enhance the rigidity of the complex, thereby improving the g_{lum} value. For $(NEt_4)_2[Eu_2(\mathbf{L_2}^S)_4]$, the helicates modified with 1-methylnaphthalene exhibit weaker C-H···π interaction due to the presence of the methyl group[49], resulting in slightly reduced rigidity compared to $(NEt_4)_2[Eu_2(\mathbf{L_1}^S)_4]$. Since the g_{CPL} value was tested in CH_3CN solution, the solid UV–vis and ^1H NMR spectra of $(NEt_4)_2[Eu_2(\mathbf{L_1}^S)_4]$ and $(NEt_4)_2[Eu_2(\mathbf{L_2}^S)_4]$ were respectively tested. It can be seen from the spectra that the solution state and crystal structure are similar (Figures S49 – S50).

To date, no universally applicable relationship has been established between CPL activity (g_{lum}) and the structures of chiral lanthanide complexes. Richardson proposed two mechanisms for explaining the origin of chiroptical activity in these complexes: static coupling and dynamic coupling mechanisms[50]. In this study, we focus solely on the impact of the static coupling mechanism on the CPL activity of lanthanide complexes. In the static coupling mechanism, the configurational chirality around the first ligand coordinating with the Ln^{3+} ion is considered. Parker et al. found a relationship between g_{lum} and the twist angle α (the angle between the top and bottom planes of the coordination polyhedron), where $g_{lum} \approx \sin 4\alpha$ for Eu(III) complexes[51–55]. According to this empirical relationship, the maximum g_{lum} value occurs when the twist angle is 22.5°, while a twist angle of 45° results in the disappearance of CPL activity. The helicate $[Yb_2(S\text{-BTHP})_4]^{2-}$, reported by our research group in 2023, typically adopts a square antiprismatic geometry (8-SAPR) coordination configuration. This helicate has an average α angle of 40.5° and exhibits a high g_{lum} value[36].

The coordination configurations of the two Eu(III) metal centers in $(NEt_4)_2[Eu_2(\mathbf{L_1}^S)_4]$ and $(NEt_4)_2[Eu_2(\mathbf{L_2}^S)_4]$ both feature a fully symmetric square antiprismatic geometry. We believe this is one of the reasons these complexes exhibit high g_{lum} values. The average α angles for $(NEt_4)_2[Eu_2(\mathbf{L_1}^S)_4]$. and $(NEt_4)_2[Eu_2(\mathbf{L_2}^S)_4]$. are 38.603° and 38.973°, respectively (Fig. 5). These angles are very close to the 40.5° twist angle of $[Yb_2(S\text{-BTHP})_4]^{2-}$, suggesting that static coupling plays a limited role in contributing to the high g_{lum} values observed in these complexes.

Conclusions

In summary, we have successfully synthesized and characterized two pairs of quadruple-stranded helicates, $(NEt_4)_2[Eu_2(\mathbf{L_1}^{R/S})_4]$ and $(NEt_4)_2[Eu_2(\mathbf{L_2}^{R/S})_4]$. Single-crystal X-ray diffraction analysis confirms the formation of homochiral quadruple-stranded dinuclear structures in both complexes. Photophysical and chiroptical investigations revealed that $(NEt_4)_2[Eu_2(\mathbf{L_1}^S)_4]$ and $(NEt_4)_2[Eu_2(\mathbf{L_2}^S)_4]$ not only exhibit intense CPL, with g_{lum} values of + 1.34 and + 1.14, respectively, but also demonstrate high luminescence quantum yields of 37.43% and 30.30%. By combining structural and chiroptical spectroscopic analyses, we propose that achieving high g_{lum} values for CPL materials in octagonal complexes requires two key factors: first, the structure must be as rigid as possible, and second, the coordination configuration should adopt a square antiprism geometry. Moreover, the relationship between g_{lum} and the twist angle α plays a crucial role in this process. This work provides valuable insights into the design of lanthanide-based CPL materials that combine both high g_{lum} values and high luminescence quantum yields.

Data availability

The datasets generated and analysed during the current study are available in the [COD] repository, [http://www.crystallography.net/cod/index.php]. The majority of data used to support the findings of this study are included in the manuscript. Additional data are available from the corresponding authors upon reasonable request.

Received: 27 January 2025; Accepted: 5 June 2025

Published online: 01 July 2025

References

1. Kim, D. Y. Potential application of spintronic light-emitting diode to binocular vision for three-dimensional display technology. *J. Korean Phys. Soc.* **49**(9), 505 (2006).
2. Tseng, M. L. et al. Stress-induced 3D chiral fractal metasurface for enhanced and stabilized broadband near-field optical chirality. *Advanced Optical Mater.* **7**(15), 1900617 (2019).
3. Grey, P. et al. Field-Effect Transistors on Photonic Cellulose Nanocrystal Solid Electrolyte for Circular Polarized Light Sensing. *Adv. Func. Mater.* **29**(21), 1805279 (2019).
4. Victor, T. W. et al. Lanthanide-binding tags for 3D X-ray imaging of proteins in cells at nanoscale resolution. *J. Am. Chem. Soc.* **142**(5), 2145–2149 (2020).
5. Wang, L. et al. Construction of a room-temperature Pt/Co/Ta multilayer film with ultrahigh-density skyrmions for memory application. *ACS Appl. Mater. Interfaces.* **11**(12), 12098–12104 (2019).
6. Kim, T. H., Cheon, S. & Yeom, H. W. Switching chiral solitons for algebraic operation of topological quaternary digits. *Nat. Phys.* **13**(5), 444–447 (2017).
7. Zheng, H. et al. Uncovering the circular polarization potential of chiral photonic cellulose films for photonic applications. *Adv. Mater.* **30**(13), 1705948 (2018).
8. Tran, A., Boott, C. E. & MacLachlan, M. J. Understanding the self-assembly of cellulose nanocrystals-toward Chiral photonic materials. *Adv. Mater.* **32**(41), 1905876 (2020).
9. Li, W. et al. Tunable upconverted circularly polarized luminescence in cellulose nanocrystal based chiral photonic films. *ACS Appl. Mater. Interfaces.* **11**(26), 23512–23519 (2019).
10. Sethy, R. et al. Enantioselective light harvesting with perylenediimide guests on self-assembled chiral naphthalenediimide nanofibers. *Angew. Chem. Int. Ed.* **56**(47), 15053–15057 (2017).
11. Yang, Y., Da Costa, R. C., Fuchter, M. J. & Campbell, A. J. Circularly polarized light detection by a chiral organic semiconductor transistor. *Nat. Photonics* **7**(8), 634–638 (2013).
12. Imai, Y., Nakano, Y., Kawai, T. & Yuasa, J. A smart sensing method for object identification using circularly polarized luminescence from coordination-driven self-assembly. *Angew. Chem.* **130**(29), 9111–9116 (2018).
13. Shuvaev, S., Suturina, E. A., Mason, K. & Parker, D. Chiral probes for α 1-AGP reporting by species-specific induced circularly polarised luminescence. *Chem. Sci.* **9**(11), 2996–3003 (2018).
14. Staszak, K., Wieszczycka, K., Marturano, V. & Tylkowski, B. Lanthanides complexes–Chiral sensing of biomolecules. *Coord. Chem. Rev.* **397**, 76–90 (2019).
15. Kawasaki, T. et al. Enantioselective synthesis of near enantiopure compound by asymmetric autocatalysis triggered by asymmetric photolysis with circularly polarized light. *J. Am. Chem. Soc.* **127**(10), 3274–3275 (2005).
16. He, C. et al. Dissymmetry enhancement in enantioselective synthesis of helical polydiacetylene by application of superchiral light. *Nat. Commun.* **9**(1), 5117 (2018).
17. Richardson, R. D. et al. Dual wavelength asymmetric photochemical synthesis with circularly polarized light. *Chem. Sci.* **6**(7), 3853–3862 (2015).
18. Sun, Z.-B.; Liu, J.-K.; Yuan, D.-F.; Zhao, Z.-H.; Zhu, X.-Z.; Liu, D.-H.; Peng, Q.; Zhao, C.-H. 2,2′-Diamino-6,6′-diboryl-1,1′-binaphthyl: A Versatile Building Block for Temperature-Dependent Dual Fluorescence and Switchable Circularly Polarized Luminescence. Angew. Chem., Int. Ed., 58, 4840–4846. (2019).
19. Guo, W. C., Zhao, W. L., Tan, K. K., Li, M. & Chen, C. F. B, N-Embedded Hetero [9] helicene Toward Highly Efficient Circularly Polarized Electroluminescence. *Angew. Chem.* **136**(18), e202401835 (2024).
20. Lee, S.; Kim, K. Y.; Jung, S. H.; Lee, J. H.; Yamada, M.; Sethy, R.; Kawai, T.; Jung, J. H. Finely Controlled Circularly Polarized Luminescence of a Mechano-Responsive Supramolecular Polymer. Angew. Chem., Int. Ed., 58, 18878–18882. (2019).
21. San Jose, B. A.; Yan, J.; Akagi, K. Dynamic Switching of the Circularly Polarized Luminescence of Disubstituted Polyacetylene by Selective Transmission through a Thermotropic Chiral Nematic Liquid Crystal. Angew. Chem., Int. Ed., 53, 10641–10644. (2014).
22. Sato, S. et al. Chiral intertwined spirals and magnetic transition dipole moments dictated by cylinder helicity. *Proc. Natl. Acad. Sci.* **114**(50), 13097–13101 (2017).
23. Shen, Z. et al. Asymmetric Catalysis Mediated by a Mirror Symmetry-Broken Helical Nanoribbon. *Nat. Commun.* **10**, 3976 (2019).
24. Jiménez, J. R. et al. Chiral molecular ruby $[Cr (dqp)_2]^{3+}$ with long-lived circularly polarized luminescence. *J. Am. Chem. Soc.* **141**(33), 13244–13252 (2019).
25. Jimeńez, J.-R. et al. Chiral Molecular Ruby $[Cr(dqp)_2]^{3+}$ with Long-Lived Circularly Polarized Luminescence. *J. Am. Chem. Soc.* **141**, 13244–13252 (2019).
26. J. L. Lunkley, D. Shirotani, K. Yamanari, S. Kaizaki and G. Muller, J. Am. Chem. Soc., 130, 13814–13815. (2008).
27. Islam, M. J. & Sharmin, N. Photofunctionalized Europium (III) complexes with circularly polarized luminescence. *Chem. Phys. Impact.* **10**, 100806 (2025).
28. Furlan, F. et al. Chiral materials and mechanisms for circularly polarized light-emitting diodes. *Nat. Photonics* **25**, 1–11 (2024).
29. Li, M. et al. Designing water-quenching resistant highly luminescent europium complexes by regulating the orthogonal arrangement of bis-β-diketone ligands. *Dalton Trans.* **50**(28), 9914–9922 (2021).
30. Liu, D. et al. Chiral BINAPO-controlled diastereoselective self-assembly and circularly polarized luminescence in triple-stranded europium (III) podates. *Inorg. Chem.* **57**(14), 8332–8337 (2018).
31. Han, G. et al. Preorganized helical chirality controlled homochiral self-assembly and circularly polarized luminescence of a quadruple-stranded $Eu_2 L_4$ helicate. *Dalton Trans.* **49**(10), 3312–3320 (2020).
32. Zhou, Y. et al. Point chirality controlled diastereoselective self-assembly and circularly polarized luminescence in quadruple-stranded europium (III) helicates. *Inorg. Chem.* **59**(17), 12850–12857 (2020).
33. Bhat, S. A. & Iftikhar, K. Samarium complexes with fluorinated β-diketone and heterocyclic Lewis bases as UV light converters. *Dyes Pigm.* **179**, 108383 (2020).
34. Li, B. et al. Insight into the roles of structures and energy levels of mono-and bis-β-diketones on sensitizing Nd (III) NIR-luminescence. *Dalton Trans.* **45**(28), 11459–11470 (2016).
35. Ahmed, Z. et al. Near infrared organic light emitting devices based on a new erbium (III) β-diketonate complex: Synthesis and optoelectronic investigations. *RSC Adv.* **7**(30), 18239–18251 (2017).
36. Ahmed, Z., Mahiya, K. & Iftikhar, K. Structures and pure near-infrared photophysics of erbium and ytterbium (III) complexes incorporating fluorinated β-diketone and neutral unidentate ligands. *New J. Chem.* **44**(30), 13172–13181 (2020).
37. Li, B. et al. Enhancement of near-infrared luminescence of ytterbium in triple-stranded binuclear helicates. *Phys. Chem. Chem. Phys.* **17**(45), 30510–30517 (2015).
38. Wang, L. et al. Remarkable 980 nm circularly polarized luminescence from dinuclear Yb(III) helicates with a D_4 symmetry. *Inorg. Chem. Front.* **10**, 3664–3674 (2023).
39. Tsurui, M. et al. Chiral Tetrakis Eu (III) Complexes with Ammonium Cations for Improved Circularly Polarized Luminescence. *Angew. Chem. Int. Ed.* **26**, e202405584 (2024).
40. Sheldrick, G. M. Crystal structure refinement with SHELXL. *Acta Crystallographica Sec. C: Struct. Chem.* **71**(1), 3–8 (2015).
41. Dolomanov, O. V., Bourhis, L. J., Gildea, R. J., Howard, J. A. K. & Puschmann, H. J. *Appl. Cryst.* **42**, 339–341 (2009).

42. Telfer, S. G., McLean, T. M. & Waterland, M. R. Exciton coupling in coordination compounds. *Dalton Trans.* **40**, 3097–3108 (2011).
43. Zhou, Y., Li, H., Zhu, T., Gao, T. & Yan, P. A Highly Luminescent Chiral Tetrahedral $Eu_4L_4(L')_4$ Cage: Chirality Induction, Chirality Memory, and Circularly Polarized Luminescence. *J. Am. Chem. Soc.* **141**, 19634–19643 (2019).
44. Wang, Y. et al. Asymmetric induction in quadruple-stranded europium (III) helicates and circularly polarized luminescence. *Dalton Trans.* **51**, 10973–10982 (2022).
45. Zhou, Y. et al. Point Chirality Controlled Diastereoselective Self-Assembly and Circularly Polarized Luminescence in Quadruple-Stranded Europium(III) Helicates. *Inorg. Chem.* **59**, 12850–12857 (2020).
46. Han, G. et al. Preorganized helical chirality controlled homochiral selfassembly and circularly polarized luminescence of a quadruple-stranded Eu_2L_4 helicate. *Dalton Trans.* **49**, 3312–3320 (2020).
47. (a) F. J. Steemers, W. Verboom, D. N. Reinhoudt, E. B. van der Tol and J. W. Verhoeven, J. Am. Chem. Soc., 1995, 117, 9408–9414; (b) M. Latva, H. Takalo, V.-M. Mukkala, C. Matachescu, J. C. Rodriguez-Ubis and J. Kankare, J. Lumin., 1997, 75, 149–169.
48. Bruce JI, Parker D, Lopinski S, Peacock RD. Survey of factors determining the circularly polarised luminescence of macrocyclic lanthanide complexes in solution. Chirality: The Pharmacological, Biological, and Chemical Consequences of Molecular Asymmetry., **14**(7):562–567. (2002).
49. Sun, J. et al. Intramolecular CH···π attraction mediated conformational polymorphism of constrained helical peptides. *Chem. Sci.* **15**(35), 14264–14272 (2024).
50. Richardson, F. S. Selection Rules for Lanthanide Optical Activity. *Inorg. Chem.* **19**, 2806–2812 (1980).
51. E. R. H. Walter, J. A. G. Williams and D. Parker, APTRA-Based Luminescent Lanthanide Complexes Displaying Enhanced Selectivity for Mg2+ , Chem. – Eur. J., 24, 7724–7733. (2018).
52. Parker, D., Dickins, R., Puschmann, H., Crossland, C. & Howard, J. Being excited by lanthanide coordination complexes: Aqua species, chirality, excited-state chemistry, and exchange dynamics. *Chem. Rev.* **102**, 1977–2010 (2002).
53. Di Bari, L., Pintacuda, G., Salvadori, P., Dickins, R. & Parker, D. Effect of axial ligation on the magnetic and electronic properties of lanthanide complexes of octadentate ligands. *J. Am. Chem. Soc.* **122**, 9257–9264 (2000).
54. Carr, R., Evans, N. H. & Parker, D. Lanthanide complexes as chiral probes exploiting circularly polarized luminescence. *Chem. Soc. Rev.* **41**, 7673–7686 (2012).
55. Dickens, R. et al. Ground and excited state chiroptical properties of enantiopure macrocyclic tetranaphthyl lanthanide complexes: controlled modulation of the frequency and polarisation of emitted light. *New J. Chem.* **22**, 891–899 (1998).

Acknowledgements

This work was financially supported by the National Natural Science Foundation of China (Nos. 52273263, 52203219 and 52073080), Scientific research project of Basic Scientific Research Operating Expenses of Colleges and Universities in Heilongjiang Province (2021-KYYWF-0029 and 2021-KYYWF-0041), Heilongjiang Provincial Natural Science Foundation Joint Guidance Projects (LH2023B022), the Natural Science Foundation of Heilongjiang(No. LH2022B014), Heilongjiang Province key research and development plan (2022ZX07D04).

Author contributions

XM.Z: Writing-original draft, Investigation, Data curation. XL.W: Data curation, Resources, Supervision. WR.H: Validation, Investigation, Supervision, Software. S.Y: Methodology, Formal analysis. T.G: Investigation, Data curation. YY.Z: Investigation, Formal analysis, Data curation, Conceptualization. HF.L: Experimental design, Writing – review & editing, Supervision, Investigation, Conceptualization. All authors reviewed the manuscript.

Funding

National Natural Science Foundation of China, 52273263, 52203219, 52073080. Scientific research project of Basic Scientific Research Operating Expenses of Colleges and Universities in Heilongjiang Province, 2021-KYYWF-0029, 2021-KYYWF-0041. Heilongjiang Provincial Natural Science Foundation Joint Guidance Projects, LH2023B022. Natural Science Foundation of Heilongjiang,LH2022B014. Heilongjiang Province key research and development plan, 2022ZX07D04.

Declarations

Competing interests

The authors declare no competing interests.

Additional information

Supplementary Information The online version contains supplementary material available at https://doi.org/10.1038/s41598-025-06053-2.

Correspondence and requests for materials should be addressed to Y.Z. or H.L.